RILEM
technical letters

Permittivity measurement of cementitious materials and constituents with an open-ended coaxial probe: combination of experimental data, numerical modelling and a capacitive model

Vincent Guihard[a,b], Frédéric Taillade[a], Jean-Paul Balayssac[b]*, Barthélémy Steck[a], Julien Sanahuja[a]

[a] 1EDF R&D, 6 quai Watier, 78401 Chatou Cedex, France
[b] 2LMDC, INSA/UPS Génie Civil 135 Avenue de Rangueil, 31007 Toulouse Cedex 04, France

Abstract

The study presents the development of a new two-dimensional FEM numerical model describing the operation of two large open-ended coaxial probes de-signed to investigate the permittivity of concrete, and its constituents. This numerical simulation, combined with a capacitive approach describing the behaviour of the probes, enabled to prove the suitability of such device to determine the permittivity of dispersive dielectrics. Finding back the permittivity of a specified material by calculation of the S parameters, change of the reference plane and use of the capacitive model is the key to the proof. Measurements performed onto different materials show good similarities with the numerical simulations. Special considerations are mentioned concerning the size of the probe and its ability to measure the permittivity of heterogeneous materials made of large inclusions. Combination of such numerical tool and measuring device can be used as a non-destructive testing technique to assess the near surface permittivity of concrete structures or as a calibration technique for GPR measurements.

Keywords: Cementitious material; Permitivity; Co-axial probe; Capacitive model; Numerical modelling

1 Introduction

The use of electromagnetic (EM) waves for the characterization of concrete moisture, either by GPR [1-3] or by capacitive methods has been investigated by many researchers. Indeed, the complex permittivity (both real and imaginary parts) of concrete is significantly influenced by moisture [4-6]. So the development of a probe able to measure complex permittivity of concrete, especially on site, is of great interest.

Moreover, Non Destructive Testing (NDT) of concrete by Ground Penetrating Radar (GPR) is a very common issue, especially for the localization of reinforcement [7-9]. On roads GPR is also used for the measurement of the thickness of pavement layers [10, 11]. For these applications, the wave velocity is required to convert the wave travel time measured by the GPR into a distance. The wave velocity is not easy to measure with usual GPR systems, especially those devoted to concrete structure investigations and so, a calibration is necessary. For instance for an accurate localization on depth of the reinforcement, drillings are done in specific points to

measure the depth of the reinforcement [12]. For roads, cores are extracted for measuring in specific points the pavement thickness assessment [13]. It is admitted that the wave velocity in a low-loss electromagnetic medium, such as concrete or pavements, is directly linked to the real part of permittivity. Then a probe which could be used on site for the assessment of dielectric constant could be useful for a fast calibration of GPR measurements and limiting drilling or cores.

One of the most popular devices to assess the permittivity of losses materials is the coaxial line based on the measurement of transmission and reflection coefficients. A material sample is inserted into a coaxial structure and the complex permittivity is derived from the analysis of the measured transmission or reflection coefficients. Several coaxial transmission lines have been developed, and their ability to characterize both real and imaginary parts of concrete permittivity on a large frequency range was demonstrated [14-16]. However, their use is mainly limited to laboratory measurements because the insertion of the sample into a coaxial line requires a specific machining of the sample not

---

easy to realize for instance on cores extracted from the structure. A coaxial-cylindrical cell without inner core was developed by Dérobert and Villain [17] which facilitates the measurement on cores [18].

Open-ended coaxial probes are an alternative to co-axial lines [19-21]. Their implementation is simple and they work in a large frequency range. However, since transmission coefficients are necessary to determine both the magnetic and dielectric properties of materials, reflection probes are essentially reserved for permittivity measurement of non-magnetic materials, like concrete.
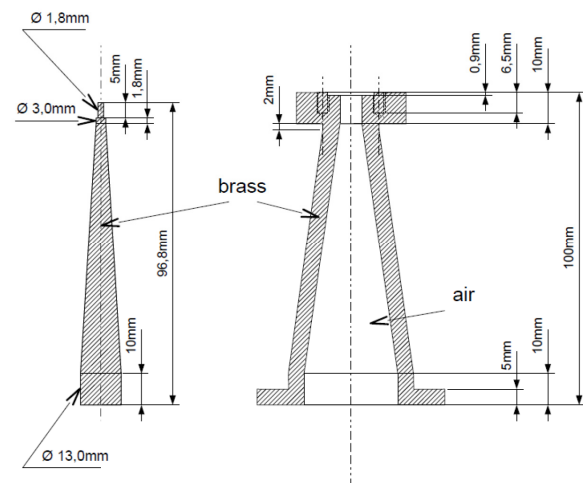
In this study we present two different sizes of probes that we have developed. A first large conical probe was designed for the investigation of concrete. The simple capacitive model used for describing the behaviour of the probe and enabling the permittivity of flat samples to be calculated is detailed. A two-dimensional axisymmetric FEM model developed to validate this approach over specific frequency ranges is presented. Then, another probe was developed for the permittivity assessment of the phases of cement paste and of the interstitial solution. The interpretation of the measurements is also performed by using the capacitive model. Permittivity values obtained on various materials (rock, sand and concrete) and on different solutions are presented.

2   Design of the large open-ended coaxial probe

Deducing the permittivity of a dielectric material from the amount of energy reflected on its surface using a coaxial probe requires the use of the transmission line theory [22]. This concept enables an accurate description of electromagnetic wave propagation through a coaxial cable and is the basis to the understanding of the probe operation. A typical coaxial cable is composed of two concentric cylindrical structures made of a conducting material (a centre core and a metallic shield) separated by a dielectric insulator. Parameters a and b will be used in the future to describe metallic core and shield radii, respectively. In such cables, transverse electromagnetic modes (TEM) are the only propagation modes allowed within the dielectric material. Thus, both electric and magnetic components of an incident wave are exclusively located within the plane perpendicular to the propagation direction. The same basic structure is used to build open-ended coaxial probes.

Figure 2. Design of the inner core (left) and metallic shield (right).

Figure 1 presents a picture of the first designed probe and the vector network analyser used during the study. The probe is characterized by a metallic core radius a = 6.5 mm and dielectric insulator radius b = 15 mm at the end of the probe. Such large diameters enable to expand the investigated volume in order to perform measurements onto heterogeneous samples characterized by large representative elementary volumes (rev) like concrete. Also, because of the device conical shape, values a and b vary along the probe length but the ratio b/a remains constant to maintain probe characteristic impedance Z_0 equal to 50 Ω and prevent any reflection phenomenon within the probe.

In Figure 2 the cross sectional view of the device is presented. Brass core and shield are kept together at the top of the probe thanks to a N connector filled with Teflon and also characterized by a 50 Ω characteristic impedance. Impedance continuity between the connector and the probe dielectrics is achieved by using different dielectric radii for the probe and connector. The device is then directly connected to a vector network analyser (VNA).

The second probe is simply built by abrading the surface of a N connector as illustrated in Figure 3. The device is characterized by a core radius a = 1.2 mm and a metallic shield radius b=4.5 mm. The smaller radii make it suitable for the study of tiny samples as well as media characterised by a small representative elementary volume.

Figure 1. Open-ended coaxial probe and VNA used during the experiments.

Figure 3. N connecter (left) and the derived open-ended coaxial probe (right).

In the present study, the analyzer is used to synthesize and deliver the electromagnetic signal which propagates within the probes towards the material under test located at its end. We now consider those probes as lossless extensions of the VNA. The only reflection phenomenon has to come from the sample placed below the probe. If the material's impedance is not equal to 50 Ω, the system made of the probe and sample is equivalent to a lossless transmission line terminated in a load impedance Z_L depending on the electromagnetic properties of the sample. This approximation is restricted to the case of semi-infinite sample i.e. deep enough to ensure that the amplitude of the electric field E is at least two orders of magnitude lower at the end of the sample than at the interface with the probe [23]. Komarov et al. [24] remind that wave propagation through the sample can be seen as a distortion of the TEM signal in the vicinity of the probe aperture. This would induce the appearance of a component of the electric field perpendicular to the aperture and a radiation of the wave into the sample. Partial reflection of the energy towards the probe is then observed.

Eq. 1 can now be used to link the S_{11} parameter, measured with the VNA, and the impedance of a sample such as,

$$\Gamma = S_{11} = \frac{Z_L - Z_0}{Z_L + Z_0} \qquad (1)$$

This reflection coefficient is known to be a function of the electromagnetic properties of the sample under test. Many models have been developed during the past decades to determine, from the measurement of a voltage reflection coefficient, the dielectric constant or the magnetic permeability of semi-infinite materials. Dielectric permittivity can sometimes be derived from the integral expression of the admittance at the end of the coaxial probe [25] for a simple system geometry. However, the vast amount of computing resource needed for its resolution makes instant measurements impossible [19]. To simplify the expression of impedance at the end of the probe, other approaches have been used like the quasi-static approach, the Taylor-series development approach or equivalent electrical circuits approaches. The latter supposes that measurement circuit is similar to a classic electrical circuit. Among those models, Chen et al. [22] remind the most famous ones: the capacitive model [23], the antenna model [26], the virtual line model [27] and the rational function model. Those models offer immediate permittivity calculation but also present drawbacks like a limited frequency range.

3   Simulation of a measurement with a two-dimensional FEM model

To validate the operation of the designed probes, it has been chosen to build a numerical model of the device and sample systems and to simulate measurements performed onto different samples. Comparison between S parameters calculated and measured for well known materials is performed.

As previously reminded, numerical simulation of this kind of probes operation has been extensively performed onto small open-ended coaxial probe [28-30]. The model proposed in this study describes the large probe mentioned above. It uses

the Finite Element Method (FEM) and is operated with COMSOL Multiphysics 5.4's RF module. The software enables resolution of the space and time dependent electric field equation. We define a port located on top of the probe as an entry port for the TEM signal to be emitted from. The software then calculates the reflection coefficient at this exact point for different signal frequencies. This reflection coefficient S_{11} depends on the electromagnetic properties attributed to the defined sample (dielectric permittivity, electrical conductivity, magnetic permeability) and is the basis to the comparison with experimental data.

3.1   Geometry building and definition of the materials' properties

In this study, we consider homogeneous or heterogeneous samples with biggest heterogeneities being small enough for the measurement to be representative. Therefore the samples defined in the numerical simulations can be represented as homogeneous. This condition enables construction of a two-dimensional axisymmetric model which drastically reduces the required computation time and power. The built geometries associated with the designed probes are presented in Figure 4.
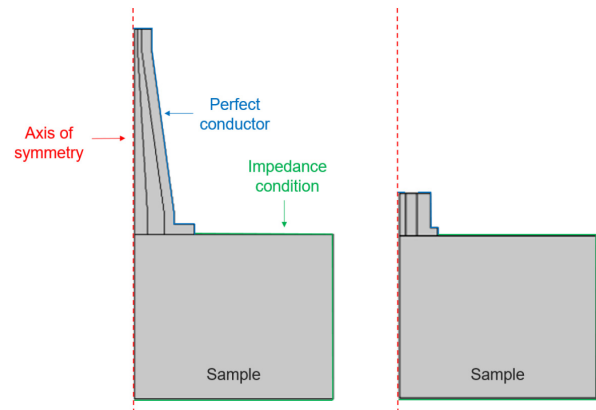

Figure 4. Built geometries and associated boundary conditions.

Dimension of every element is chosen to be equal to the real probes dimensions, except for dimensions of the sample below, which can be adjusted. It is then possible to assign the different properties to each of the elements, and for the entire frequency range set, as presented in Table 1.

Table 1. Electromagnetic properties assigned to each element of the numerical model

Element	ϵ (SI)	σ (S/m)	μ (SI)
Core (brass)	1	$71 \cdot 10^9$	1
Insulator (air)	1	0	1
Shield (brass)	1	$71 \cdot 10^9$	1
Sample	ϵ_r	σ_r	1

We also define limit conditions at the boundaries of the system. Perfect conductor conditions are applied all around the metallic parts of the probe (Figure 4) and impedance boundary conditions are applied at the outer parts of the sample. The simulation is then performed for specific TEM waves emitted from the port for a given set of frequencies like

with any open-ended coaxial probe. As a very broadband method, it is worth calculating reflection coefficients for a wide frequency spectrum defined here as [1 MHz; 2 GHz] (100 calculations are incorporated within these ranges). Computation time required to calculated S_{11} parameters over such frequency range is less than ten seconds.
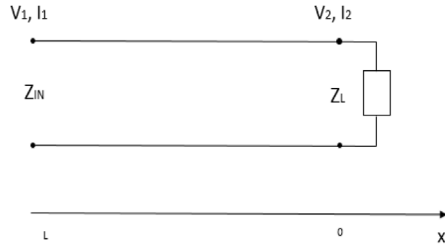
3.2   Change of reference plane

Figure 5. Change of reference plane in a transmission line.

S_{11} parameters being calculated at a precise position defined as the emission port of the device (top of the probe), one has to apply a transmission matrix to the calculated parameters in order to evaluate the reflected parameters at the interface between the probe and the material under test. This can only be done by assuming that the probe is a lossless transmission line and by knowing the exact length of the probe as well as the permittivity of the dielectric material filling-in the probe (air).

S parameters at the load S_{11}^L can then be calculated according to the S parameters at the entrance of the probe S_{11}^{IN}, the signal frequency f, its velocity v and the probe length L,

$$S_{11}^2 = S_{11}^1 e^{2j\frac{v}{f}L} \qquad (2)$$

4   Comparison with experimental results and introduction of the capacitive model

4.1   Measurement procedure

The vector network analyzer used in this study is an Anritsu MS46121A with a signal frequency range set to [1 MHz; 2 GHz]. Measurement of the S_{11} parameter over this broad range was performed onto materials with known permitivities like air, Teflon and also onto materials with unknown electromagnetic properties like rock aggregate, sand or concrete samples.

A calibration procedure of the VNA is required before setting up the probe in order to take into account external factors influencing the device operation like temperature or hygrometry. This is performed by measuring the reflected signal onto three different loads (open circuit, short circuit and a 50 Ω load impedance).

It is also necessary to remind that the default configuration of the reference plane of the VNA after calibration is defined at the output of the device. S_{11} parameters will be measured at this exact position. In the present study, measurement of this reflection coefficient has to be performed at the boundaries of the load impedance i.e. at the interface between the probe and the sample. This is necessary because the impedance (deduced from the S parameter) measured at the entry of a

transmission line (Z_{in} on Figure 5) differs from the impedance at the boundaries of the load (Z_L). This is due to the phase deploying itself over the additional line length induced by the probe. Change of reference plane is performed by plugging the probe in, short-circuiting it by placing a conductive material at its end like a copper foil. Thanks the VNA software, the coefficient βl that cancels the new phase introduced is searched and the reference plane is adjusted.

4.2   S parameters measured and calculated

Firstly, one compares the S_{11} parameters obtained from FEM calculations and from measurements performed on a well-known material, in the case of a 6.5 mm core radius open-ended probe. The permittivity of Teflon is known to be ϵ_{teflon} = 2.1 + 0j within the studied frequency range. We set values within the range [1.9; 2.4] as the dielectric constant for the sample under test on the simulation as well as 0 for the electric conductivity and 1 for the permeability. Module and phase of the S_{11} calculated at the interface between sample and probe are then compared to the one measured on a Teflon block. Measurements have been performed for five different positions above the Teflon sample. The mean value as well as the corresponding error are presented on Figure 6 and 7 over the frequency range [1MHz; 4GHz].
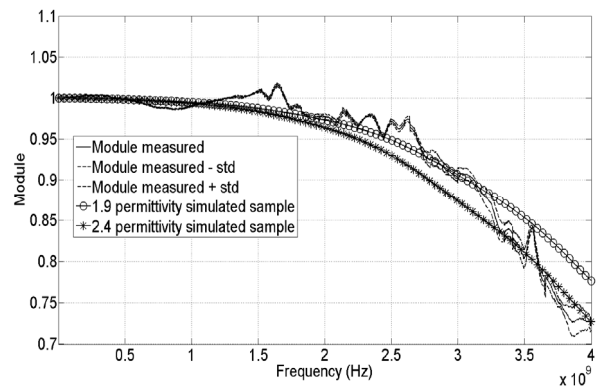

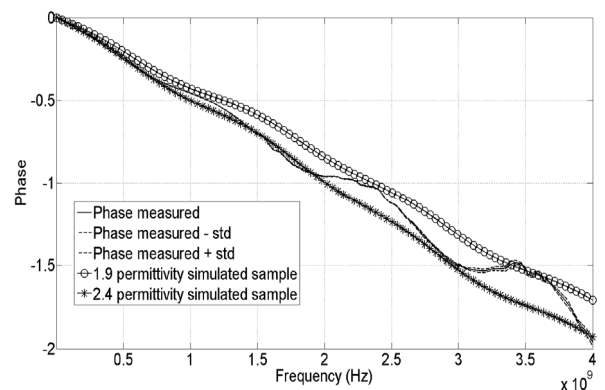**Figure 6.** Comparison between experimental and calculated modules of a Teflon sample.

Figure 7. Comparison between experimental and calculated phases of a Teflon sample.

Even though a good measurement reproducibility is observed, no distinction can be made between materials with permittivity lying between 1.9 and 2.4 and the measured

signal. Mean squared root for measured parameters and calculated ones with permittivity equal to 1.9 and 2.4 are found to be equal to 0.8. The same behaviour has been observed with air as a sample. To overcome this lack of accuracy, one can use the capacitive model that requires two reference materials to calculate permittivity of an unknown material from their S_{11} parameters.

4.3   Introduction of the capacitive approach
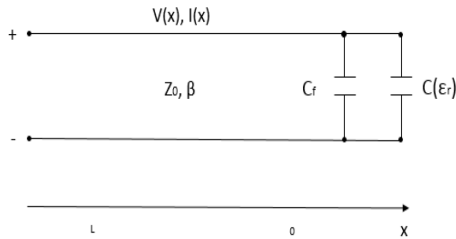
Figure 8. Electrical equivalent circuit of a coaxial probe and dielectric sample according to the capacitive model.

A picture of the capacitive model electrical circuit is presented on Figure 8. This circuit is made of two capacitors C_f and $C(\epsilon_r^*)=\epsilon_r^*\chi$ connected in parallel. Capacitor $C(\epsilon_r{}^*)$ is used to model the electric energy storage capacity of the sample. The complex value of the permittivity ϵ_r^* enables the consideration of dielectric losses within the material. The χ factor is a geometric factor used to take into account the geometry of the probe. Eventually, the capacitor C_f is often used to interpret the energy storage capacity due to the fringing fields. This capacity is material independent and only comes from the fact that fringing fields exist at the boundaries of every non-infinite planar capacitors [31]. Parameters χ and C_f being difficult to estimate, a calibration procedure using well-known materials is necessary.

Using Eq. 1, an expression describing permittivity of a sample placed at the end of the coaxial probe can be deduced,

$$\epsilon_r^* = \frac{1-S_{11}}{j\varpi Z_0\chi(1+S_{11})} - \frac{C_f}{\chi} \qquad (3)$$

It is possible to get rid of the two unknown parameters Cf and χ by measuring the S11 parameter on two materials of known permittivity ϵ_1^{ref} and ϵ_2^{ref}. The resulting expression for the dielectric constant of a random sample is therefore given by,

$$\epsilon_r^* = \epsilon_1^{ref} + \left(\epsilon_2^{ref} - \epsilon_1^{ref}\right)\left(\frac{Y_r-Y_1^{ref}}{Y_2^{ref}-Y_1^{ref}}\right) \qquad (4)$$

We used in this study as reference materials air $\epsilon_{air} = 1 + 0j$ and a 25×15×10 cm^3 Teflon block ϵ_{teflon} = 2.1 + 0j). The third material investigated is the one with unknown properties. Following the previously described procedure, one can convert S_{11} spectrum into a permittivity dispersion spectrum. Figures 9 and 10 present the permittivity spectra obtained with the largest probe (core radius a = 6.5 mm) for Teflon as the unknown sample. The accuracy of the deduced permittivity is drastically improved since the obtained spectrum indicates a permittivity lying between 2.1 and 2.2. Mean squared root calculated is here equal to 0.05 when using 2.1 and 2.2 permittivity for the simulated material. The capacitive model as well as the measurement process are

here validated over the frequency range [1MHz; 2GHz] for the largest probe.
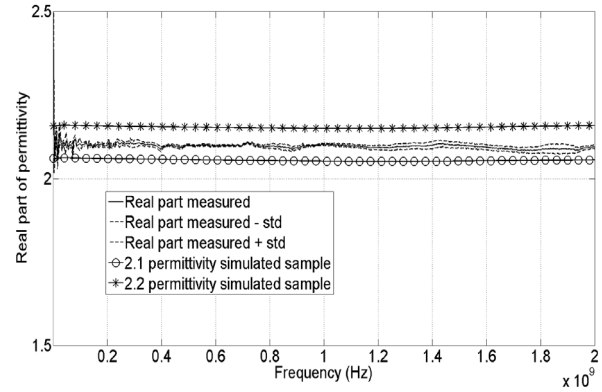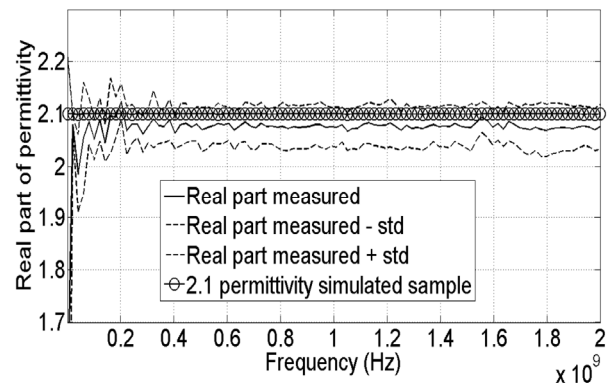

Figure 9. Real part of the permittivity of Teflon measured and simulated with core radius a = 6.5 mm.
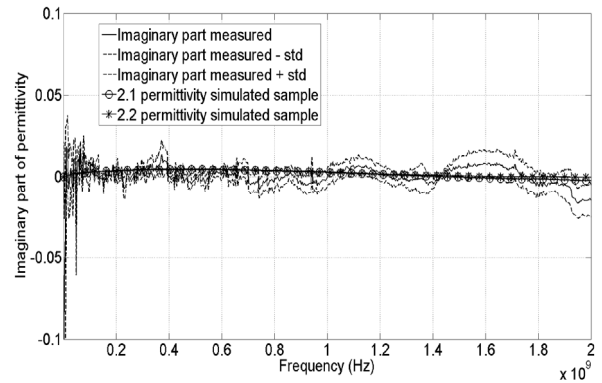
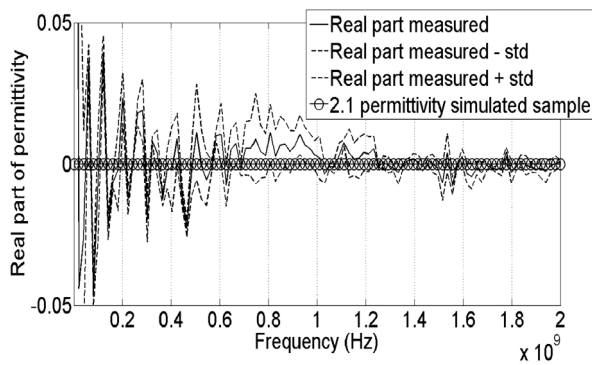**Figure 10.** Imaginary part of the permittivity of Teflon measured and simulated with core radius a = 6.5 mm.

The same measurement and simulation procedures are applied with the 1.2 mm core radius probe on the same Teflon sample. Estimated permittivity is presented in Figure 11 and 12 in terms of real and imaginary parts. A close match between measurement, simulation and theoretical permittivity is observed.

Figure 11. Real part of the permittivity of Teflon measured and simulated for the probe with core radius a = 1.2 mm.
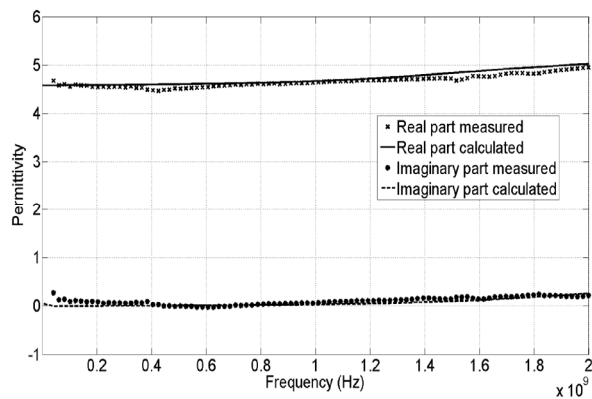
Figure 12. Imaginary part of the permittivity of Teflon measured and simulated for the probe with core radius a = 1.2 mm.

It can be therefore concluded that a combination of a probe measurement and an iteration process comparing calculation results and measurements can be used to deduce the permittivity of any flat medium including cementitious materials or their components.

5 Comparison with experimental results and introduction of the capacitive model

## 5.1 Permittivity of a rock sample

Figure 13. Measurement of the real and imaginary parts of the permittivity of an aggregate sample compared to a 4.6 permittivity simulated material.

The unknown material investigated here is a homogeneous 14×7×9 cm3 aggregate block commonly used as one of the components of concrete. The frequency range chosen is [1 MHz; 2 GHz]. Permittivity spectrum deduced from the measurement of the S parameters onto its flat surface with the 6.5 mm core radius open-ended coaxial probe is presented on Figure 13. The real part lies between 4 and 5 at low frequencies and slightly increases at high frequencies. The imaginary part is almost equal to 0 at low frequencies and also seems to increase at high frequencies. The material is supposed to be homogeneous and flat enough to enable measurements with an open-ended coaxial probe. Permittivity deduced from the measurement of reflection coefficient is also compared to the results of simulations for fictive materials with permittivity comprised between 4 and 5. It is found that the minimum mean squared root and thus the best overlapping between experimental and calculated properties is obtained for the simulated sample with

permittivity ϵ_r = 4.6 (Figure 13). We observe on both the numerical simulation and the measurement an increase in the permittivity value for high frequencies. Such artefact is found to be dependent on the probe geometry as well as the permittivity of the dielectric material filling the probe. The larger the probe's diameter, the stronger the shift in permittivity. This shift decreases for small diameters and when the permittivity of the dielectric filler is close to the sample's one, resulting in a lower impedance discontinuity. We hence conclude that this effect is caused by the probe geometry itself, since it is observed on both simulated and measured data and should not be taken into account. Once again, it can be concluded that the built model can be used to accurately determine the permittivity of samples thanks to an iteration process comparing results from measurements and calculations and minimizing their mean squared root.

5.2 Permittivity of an unsaturated sand

The same approach is used to determine the permittivity of an unsaturated sand made up by crushing the previously described rock sample. Figure 14 presents the real part of the permittivity obtained with the 6.5 mm core radius open-ended coaxial probe for three different saturation degrees (0%, 30% and 60%). Water's dielectric constant being way higher than the solid part's one, a permittivity increase is observed along with the water content. Because of ionic species present within the saturating water, a dispersive behaviour appears at sufficiently low frequencies for the imaginary part (Figure 15). Its magnitude is a function of the amount of ions present within the wetting medium.
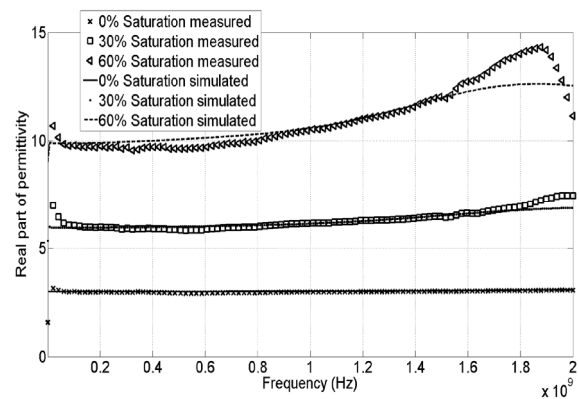
Figure 14. Real part of the permittivity measured (lines) and calculated (dots) for different saturations.
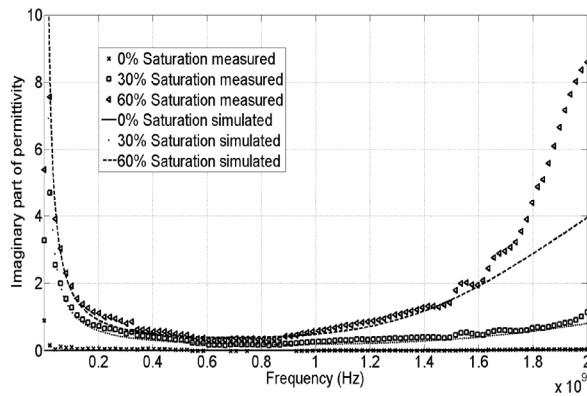
Figure 15. Imaginary part of the permittivity measured (lines) and calculated (dots) for different saturations.

It can also be observed that the permittivity shift caused by the measuring system and by the model used is increasing as the permittivity value of the material under test is distant from the permittivity of the dielectric filling the probe (here air). This deviation should not be taken into account as it appears in both measurements and simulations in the same way. An iteration process comparing set and measured permittivity is used to conclude about sample's electromagnetic properties.

Best overlapping is obtained for simulated samples with the properties as presented in Table 2.

Table 2. Electromagnetic properties of the simulated samples.

Saturation	ϵ (SI)	σ (S/m)	μ (SI)
0%	3	0	1
30%	6	$6.7 \cdot 10^{-3}$	1
60%	10	$10 \cdot 10^{-3}$	1

5.3   Permittivity of concrete samples

Figure 16 presents the permittivity measured over the range [1 MHz; 2 GHz] of a concrete sample estimated with the 6.5 mm core radius open-ended coaxial probe. Sample's height is equal to 5 cm and radius is 11 cm. The cylinder has been dried in an oven at 100 °C for 30 days. The real part of the sample's permittivity lies around 6 at low frequencies and increases at high frequencies. Its imaginary part is equal to zero at low frequencies and also increases at high frequencies. Figure 16 also presents the calculated permittivity for a simulated sample with a dielectric constant equal to 6.1. We can thus deduce that concrete permittivity is approximately equal to 6.1. This result is consistent with some measurements performed with different techniques [32, 21].
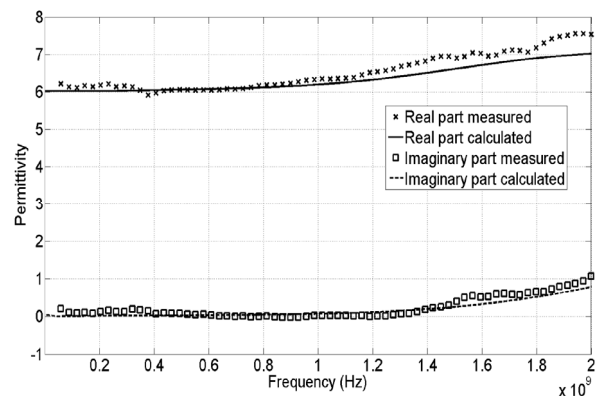
Figure 16. Measurement of the real and imaginary parts of the permittivity of a concrete sample compared to a simulated material (permittivity set at 6).

5.4   Permittivity of a concrete's interstitial solution

The amount of interstitial solution present within concrete's pores as well as its ionic composition influence the effective permittivity of the heterogeneous material. Measurements were performed with the 1.2 mm core radius open-ended coaxial probe on a recreated concrete's interstitial liquid. Even though interstitial liquid composition vary from one concrete to another, results presented below prove the ability of the designed probe to estimate its dielectric dispersion over the frequency range [1 MHz; 2 GHz]. The interstitial liquid used was recreated from the dosing of the liquid extracted from a CEM-I concrete, as presented in [33]. A large enough volume was synthesized in order to perform a permittivity measurement. Molar concentration of each chemical specie is presented in Table 3.

Table 3. Composition of the synthesized interstitial solution based on the dosing of a CEM-I concrete recreated in a previous study [33].

Na^+ (mol/m^3)	K^+ (mol/m^3)	OH^- (mol/m^3)
31.5	122.8	154.3

As an input for the numerical simulation procedure, DC conductivity σ of the liquid was measured with a conductivity meter and we obtained σ=3.32 S/m. A static dielectric constant ϵ_r=80 was chosen as the dielectric permittivity of the sample. Simulated dielectric permittivity was then compared with a Debye equation classically used to model the dielectric dispersion of conductive water below 100 GHz [34] and defined as,

$$\epsilon = \epsilon_\infty + \frac{\epsilon_{stat} - \epsilon_\infty}{1 + i\varpi\tau} + \frac{\sigma}{i\varpi\epsilon_0} \qquad (5)$$

where ϵ_{stat} and ϵ_∞ are the limit of permittivity at low and high frequencies, respectively equal to 80 and 3.13. τ is the relaxation time of pure water (τ =10^{-11} s and ϵ_0 the permittivity of free space. Experimental and numerically derived results are presented along with the Debye model in Figure 17. Similar behaviour is observed between measurement and simulation of both real and imaginary part of permittivity.
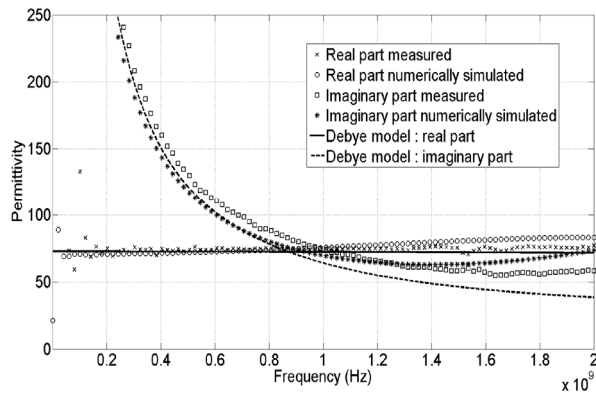
Figure 17. Measured and simulated permittivity of a concrete's interstitial liquid. Comparison with a Debye model.
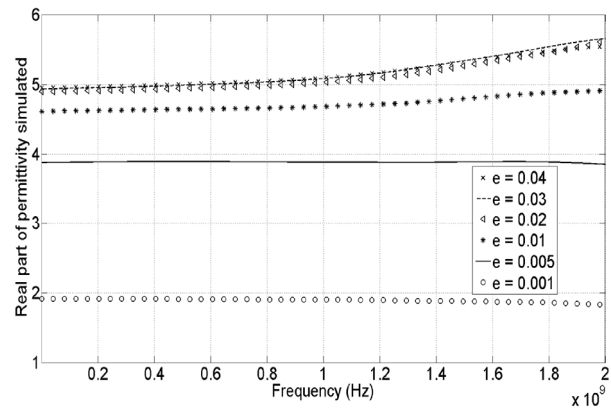

Figure 18. Real part of the calculated permittivity of samples with different thicknesses e (m).

6 Determination of probe's intrinsic and related parameters

6.1 Effective penetration depth

Many experiments have been performed in order to estimate the effective penetration depth of waves in a sample during open-ended coaxial probe measurement [30, 35-37]. This effective penetration depth is closely related to the probe's diameter [35] and is in the same order of magnitude as this diameter [30].   Meany et al. [35] computed the evolution of the penetration depth as a function of probe diameter, frequency and medium permittivity. Probe diameter is found to be the most influential parameter and penetration depth is almost constant with frequency and sample permittivity. The effective penetration depth is an important characteristic especially when dealing with heterogeneous samples like concrete. Care must be taken when studying materials with such large heterogeneities. A probe with a large diameter is necessary to study concrete samples including aggregates of a few centimetres.

Figure 18 presents the real part of the permittivity resulting from a simulation performed for the 6.5 mm core radius probe with a heterogeneous sample made of two layers with a different permittivity. We aim to estimate the wave penetration depth. The upper layer is made of a material with permittivity $5 + 0j$. The lower material is air ($\epsilon = 1 + 0j$). We compute the effective permittivity following the described procedure for different sample thicknesses e. Results show that for samples with permittivity $5 + 0j$ thinner than 2 cm, the resulting permittivity is different than $5 + 0j$. Effective penetration depth hence lies around 2 cm.

6.2 Effect of an air gap between the probe and the sample

Effect of an air gap between the probe and the material's surface also needs to be considered. This effect has been studied and modelled by Baker at al. [36]. It has been observed experimentally by measuring the permittivity of a Teflon block dipped into a liquid and getting away from the probe by Meaney et al. [37]. Critical effects are observed for sub millimetres gaps and non-linear evolution from Teflon permittivity to water permittivity is recorded and simulated. This is why it is sometimes not recommended to use open-ended coaxial probes with solid because of the surface roughness inducing air gaps and permittivity shifts. Using the two-dimensional model for the 6.5 mm core radius probe, we simulated the effect of an air gap introduced between the sample and the probe. The modelled sample is now made of two layers with different permittivities. The top material has air's dielectric constant ($1 + 0j$). The permittivity of the bottom material is chosen to be $5 + 0j$. The simulation is performed with different air layers (sample's depth remains constant and equal to 5 cm). The real part of the permittivity deduced from such numerical simulations are present on Figure 19 for the frequency range [1 MHz ; 2 GHz].
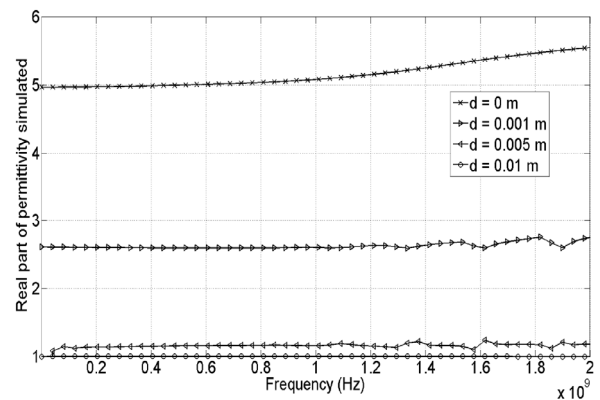

Figure 19. Real part of the calculated permittivity of a sample separated from the probe by an air layer d (m).

One can notice that a 1 mm gap is enough to induct a shift in the calculated permittivity of almost half the true value. It is also noticed that when the air layer is larger than 1 cm, the calculated permittivity is equal to 1. The sample itself does not have any effect on the measurement any more. It should be noted that this value depends on the sample permittivity.

7   Conclusion

The current work focuses on validating a new large probe, and a simple capacitive model describing the device's behaviour and ability to determine the dielectric permittivity of civil engineering materials. The open-ended coaxial probe used was connected to a vector network analyser Anristu MS46121A operating at frequencies ranging from 1 MHz to 2 GHz. A good agreement between experimental data and a new two-dimensional axisymmetric FEM model of the developed system proves the suitability of the method to calculate the permittivity of homogeneous and heterogeneous flat dispersive dielectrics. The process described presents the device as a promising way to determine the permittivity of civil engineering materials and their structural phases. Measurement were performed on different materials including concrete and some of its components (rock aggregate, sand, interstitial liquid).

Future perspectives could focus on the development of probes directly immersed into concrete structures to avoid effects of an air gap between the sample and the probe. Results can also be used to design new probes suiting different materials in terms of their size or the size of their heterogeneities.

References

[1]   S. Laurens, J.P. Balayssac, J. Rhazi, G. Arliguie. Influence of concrete relative humidity on the amplitude of ground-penetrating radar (GPR) signal. Mater Struct   (2002) 35:198–203.
https://doi.org/10.1007/BF02533080

[2]   X. Dérobert, J. Iaquinta, G. Klysz, J.P. Balayssac. Use of capacitive and GPR techniques for the non-destructive evaluation of cover concrete. NDT & E Int (2008) 41:44–52.
https://doi.org/10.1016/j.ndteint.2007.06.004

[3]   W.L. Lai, S.C. Kou, W.F. Tsang, C.S. Poon. Characterization of concrete properties from dielectric properties using ground penetrating radar. Cem Concr Res (2009) 39(8):687–695.
https://doi.org/10.1016/j.cemconres.2009.05.004

[4]   G. Klysz and J.P. Balayssac. Determination of volumetric water content of concrete using ground-penetrating radar. Cem Concr Res (2007) 37:1164–1171.
https://doi.org/10.1016/j.cemconres.2007.04.010

[5]   T. Kind, S. Kruschwitz, J. Wöstmann, S. Wiggenhauser. Spectral absorption of spatial and temporal ground penetrating radar signals by water in construction materials. NDT & E Int (2009) 67:55–63.
https://doi.org/10.1016/j.ndteint.2014.06.009

[6]   M. Sbartai, S. Laurens, J.P. Balayssac, G. Ballivy, and G. Ballivy. Ability of the direct wave of radar ground-coupled antenna for NDT of concrete structures. NDT & E Int (2006) 39(5):400–407.
https://doi.org/10.1016/j.ndteint.2005.11.003

[7]   J.H. Bungey. Sub-surface radar testing of concrete: a review. Constr Build Mater (2004) 18(1):1–8. https://doi.org/10.1016/S0950-0618(03)00093-X

[8]   E. Carrick Utsi. Ground Penetrating Radar, Theory and Practice. Elsevier, 2017.

[9]   K. Dinh, N. Gucunski, and T. Zayed. Automated visualization of concrete bridge deck condition from GPR data. NDT & E Int (2018) 102:120–128. https://doi.org/10.1016/j.ndteint.2018.11.015

[10]   ASTM international D6087-08. Standard test method for evaluating asphalt-covered concrete bridge decks using ground penetrating radar, 2015.

[11]   ASTM international D4748-10. Standard test method for determining the thickness of bound pavement layers using short-pulse radar, 2015.

[12]   A. Tarussov, M. Vandry, A. De La Haza. Condition assessment of concrete structures using a new analysis method: Groundpenetrating radar computer-assisted visual interpretation. Constr Build Mater (2013) 38:1246–1254.
https://doi.org/10.1016/j.conbuildmat.2012.05.026

[13]   L. Edwards, H.P. Bell. Comparative evaluation of nondestructive devices for measuring pavement thickness in the field. Int J Pavement Res Technol (2016) 9(2):102–111.
https://doi.org/10.1016/j.ijprt.2016.03.001

[14]   I.L. Al-Qadi, S.M. Riad, R. Mostaf, W. Su. Design and evaluation of a coaxial transmission line fixture to characterize portland cement concrete. Constr Build Mater (1997) 11(3):163–173.
https://doi.org/10.1016/S0950-0618(97)00034-2

[15]   A. Robert. Dielectric permittivity of concrete between 50 MHz and 1 GHz and GPR measurements for building materials evaluation. J App Geophys   (1998)   40:89–94.   https://doi.org/10.1016/S0926-9851(98)00009-3

[16]   M. Soutsos, J.H. Bungey, S.G. Millard, M.R. Shaw, D.A. Patterson. Dielectric properties of concrete and their influence on radar testing. NDT & E Int (2001) 34:419–425. https://doi.org/10.1016/S0963-8695(01)00009-3

[17]   X. Dérobert, G. Villain. Development of a multi-linear quadratic experimental design for the em characterization of concretes in the radar frequency-band. Constr Build Mater (2017) 136(1):237–245.
https://doi.org/10.1016/j.conbuildmat.2016.12.061

[18]   G. Villain, V Garnier, Z.M. Sbartai, X. Dérobert, J.P. Balayssac. Development of a calibration methodology to improve the on-site non-destructive evaluation of concrete durability indicators. Mater Struct (2018) 51(40):237–245.
https://doi.org/10.1617/s11527-018-1165-4

[19]   B. Filali, F. Boone, J. Rhazi, G. Ballivy. Design and calibration of a large open-ended coaxial probe for the measurement of the dielectric properties of concrete., IEEE Transactions on Microwave Theory and Techniques (2008) 56:2322 – 2328.
https://doi.org/10.1109/TMTT.2008.2003520

[20]   S. van Damme, A. Franchois, D. De Zutter, L. Taerwe. Nondestructive determination of the steel fiber content in concrete slabs with an open-ended coaxial probe. IEEE Transactions on Geoscience and Remote Sensing (2009) 42:2511–2521.
https://doi.org/10.1109/TGRS.2004.837332

[21]   F. Demontoux, S. Razafindratsima, S. Bircher, G. Ruffie, F. Bonnaudin, F. Jonard, J.P. Wigneron, Z.M. Sbarta, Y. Kerr. Efficiency of end effect probes for in-situ permittivity measurements in the 0.5-6Ghz frequency range and their application for organic soil horizons study. Sensors and Actuators A: Physical (2016) 254:78–88.
https://doi.org/10.1016/j.sna.2016.12.005

[22]   L.F. Chen, C.K. Ong, C.P. Neo, V.V. Varadan, V.K. Varadan. Microwave Electronics: Measurement and Materials Characterization. Wiley, 2004. https://doi.org/10.1002/0470020466

[23]   M. Stuchly S. Stuchly. Coaxial line reflection methods for measuring dielectric properties of biological substances at radio and microwave frequencies-a review. Instrumentation and Measurement, IEEE Transactions on, 29:176 – 183, 10 1980.

[24]   S. A. Komarov, A. Komarov, D. G. Barber, M. Lemes, S. Rysgaard. Openended coaxial probe technique for dielectric spectroscopy of artificially grown sea ice. IEEE Transactions on Geoscience and Remote Sensing, 54:1–11, 08 2016.

[25]   D. K. Misra. A quasi-static analysis of openended coaxial lines (short paper). IEEE Transactions on Microwave Theory and Techniques (1987) 35:925–928. https://doi.org/10.1109/TIM.1980.4314902

[26]   M. Brandy, S. Symons, S. Stuchly. Dielectric behavior of selected animal tissues in vitro at frequencies from 2 to 4 Ghz. IEEE Transactions on Biomedical Engineering (1981) 28:305 – 307.
https://doi.org/10.1109/TBME.1981.324707

[27]   F.M. Ghannouchi R. Bosisio. Measurement of microwave permittivity using a six-port reflectometer with an openended coaxial line. IEEE Transactions on Instrumentation and Measurement (1989) 38:505–508. https://doi.org/10.1109/19.192335

[28]   N.I. Sheen and I. Woodhead. An open-ended coaxial probe for broad-band permittivity measurement of agricultural products. J Agricult Eng Res (1999) 74:193–202. https://doi.org/10.1006/jaer.1999.0444

[29]   A. Jusoh, Z. Abbas, M.A. Abd Rahman, C. Meng, M. Zainuddin, F. Esa. Critical study of open ended coaxial sensor by finite element method (FEM). Int J App Sci Eng (2014) 11(4).

[30] M. Adous. Caractérisation électromagnétique des matériaux traités de génie civil dans la bande de fréquence 50 MHz 13 GHz. PhD thesis, Université de Nantes, 2006.

[31] V. Leus, D. Elata. Fringing effect in electrostatic actuators. Technical report, Israel Institute of Technology, Faculty of Mechanical Engineering, 2004.

[32] X. Dérobert, G. Villain, R. Cortas,J.L. Chazelas. EM characterization of hydraulic concretes in the GPR frequency band using a quadratic experimental design. Non-Destructive Testing in Civil Engineering Nantes, France, 06 2009.

[33] W. Ali Mze. Évaluation non destructive de la contamination du béton par les chlorures avec la technique radar. PhD thesis, Université Paul Sabatier Toulouse III, 2018.

[34] P. Debye. Polar molecules. The Chemical Catalog Compan, 18, 1929.

[35] P. M. Meaney, A. Gregory, J. Seppala, T. Lahtinen. Open-ended coaxial dielectric probe effective penetration depth determination. IEEE Transactions on Microwave Theory and Techniques (2016) 64:1–9. https://doi.org/10.1109/TMTT.2016.2519027

[36] J. Baker-Jarvis, M.D. Janezic, P. D. Domich, R. G. Geyer. Analysis of an open-ended coaxial probe with lift-off for non-destructive testing. IEEE Transactions on Instrumentation and Measurement (1994) 43:711–718. https://doi.org/10.1109/19.328897

[37] P. M. Meaney, A. Gregory, N. Epstein, K. D. Paulsen. Microwave open-ended coaxial dielectric probe: Interpretation of the sensing volume re-visited. BMC Medical Physics (2014) 14. https://doi.org/10.1186/1756-6649-14-3